Supplementary Materials for

Hox Genes Regulate Digit Patterning by Controlling the Wavelength of a Turing-Type Mechanism

Rushikesh Sheth, Luciano Marcon, M. Félix Bastida, Marisa Junco, Laura Quintana, Randall Dahn, Marie Kmita,* James Sharpe,* Maria A. Ros*

*To whom correspondence should be addressed. E-mail: marian.ros@unican.es (M.A.R.); james.sharpe@crg.eu (J.S.); marie.kmita@ircm.qc.ca (M.K.)

Published 14 December 2012, *Science* **338**, 1476 (2012)
DOI: 10.1126/science.1226804

This PDF file includes:

Contents

1 Materials and Methods

Whole mount *in situ* hybridization was performed as previously described [33] using probes directed against mouse *Sox9*, *Hoxd13*, *Hoxd12* and *Coll21a* (kindly provided by Denis Duboule, and Susan Mackem).

Whole-mount skeletal preparations were performed by staining with Alizarin Red and Alcian blue following standard protocols.

All measurements were performed in pictures taken from specimens in PBS after whole mount *in situ* hybridization. Although the process of dehydration shrinks the tissue, the posterior rehydration brings it back to the previous size [34].

2 Supplementary text - Modeling details

List of Figures

List of Tables

2.1 Introduction

Three qualitative behaviors support a self-organizing mechanism in contrast to a positional information model for the specification of the digit pattern:

- More digits are formed when the developmental field is increased. This can be seen in Figure 1A by comparing the WT skeletal pattern with that of the *Gli3 -/-* mutant that has a bigger autopod and more digits.
- Progressive allele removal of a strongly related family of genes (distal *Hox* genes) induces the formation of an increased number of thinner digits within the same space.
- Distal digit bifurcations occur.

These observations are difficult to explain with a positional information model and are consistent with the hypothesis that distal *Hox* genes control a self-organizing mechanism responsible for the periodic patterning of digits. Furthermore, Turing models have frequently been criticized on the grounds that they predict significant variability in phenotypic result, and therefore do not display the robustness perceived to be inherent in developmental mechanisms. The observed variability in digit number and digit bifurcations within each genotype analyzed in this study provides an important counter-argument, as it highlights that some naturally-evolved developmental systems may be less robust than sometimes imagined.

The quantification showed in Figure 4B-C reveals that from the *Hoxa13 +/+; Hoxd11-13 +/+* mutant to the *Hoxa13 +/-; Hoxd11-13 -/-* mutant the average digit period is reduced of 1.5 times. Figure 1C and Figure 4B highlight that within each limb the average digit period is increased from the proximal to the distal boundary of the autopod. This scaling is reduced when *Hox* genes are removed and distal digit bifurcations are observed. In addition, two other phenomena are observed when distal *Hox* genes are removed:

- The formation of the skeletal pattern is delayed. This is highlighted in Figure S2 where the skeletal patterns of the *Gli3 +/- ; Hoxa13 +/-; Hoxd11-13 -/-* mutant and the *Gli3 -/- ; Hoxa13 +/-; Hoxd11-13 -/-* mutant are compared with the patterns of the *Gli3 -/-* and the *Gli3 +/-* mutant at a similar stage.

- The PD length of the distal region is reduced. This is showed by the *Sox9* hybridizations in Figure 3 and confirmed at later stages by *Col2a* hybridizations, see the Figure S3.

From the quantification we formulated the following hypothesis:

- *Hox* genes increase the wavelength of a self-organizing mechanism.

- *Hox* genes increase the speed of pattern appearance.

- *Hox* genes increase the wavelength in a PD graded manner and control the PD width of the digits.

To investigate these hypothesis we analyzed the behavior of a general two dimensional reaction-diffusion model that is able to self organize to produce a periodic pattern. Alternatively, a self-organizing mechano-chemical model based on cellular re-organizations could be considered. However, recent results [37] highlighted that very limited change in cellular properties is observed at early times after skeletal pattern specification. Moreover, previous studies [11][40] showed that mechano-chemical models capable of forming periodic patterns are mathematically equivalent to reaction-diffusion models. Therefore, we are confident that our results could be easily related to more complex models that include change in cellular behavior.

2.2 The Turing reaction-diffusion model

We considered a general reaction-diffusion model made of two reactants u and v in the form:

$$\begin{aligned} \frac{\partial u}{\partial t} &= f(u,v) + d_u \nabla^2 u \\ \frac{\partial v}{\partial t} &= g(u,v) + d_v \nabla^2 v \end{aligned} \tag{1}$$

The biological implementation of the reaction kinetics f and g is unknown. For this reason, we used the general model developed in [25] that is obtained by linear approximation around the steady state $(0,0)$. In addition, a cubic term (u^3) was used to limit the growth of the activator. We obtained f and g in the form:

$$\begin{aligned} f(u,v) &= f_u u + f_v v - u^3 \\ g(u,v) &= g_u u + g_v v \end{aligned} \tag{2}$$

Any reaction-diffusion model of two species can be approximated to this general form by Taylor expansion up to the cubic term. According to [43] this model produces a diffusion-driven instability when the following conditions are satisfied:

$$\begin{aligned} f_u + g_v < 0, \quad & f_u g_v - f_v g_u > 0 \\ d_u f_u + d_v g_v > 0, \quad & (d_v f_u + d_u g_v)^2 - 4d(f_u g_v - f_v g_u) > 0 \end{aligned} \tag{3}$$

The parameters showed in Table ST1 that just satisfies the condition (3) were used as a starting point for our analysis.

f_u	f_v	g_u	g_v	d_u	d_v
0.49	-0.5	0.5	-0.5	70	875

Table ST1: The parameter set used, the spatial unit is μm

This parameter set represents an Activator-Inhibitor model where u is an activator that auto-activates itself and promotes its own inhibitor (v). The corresponding network diagram is shown in Figure S7.

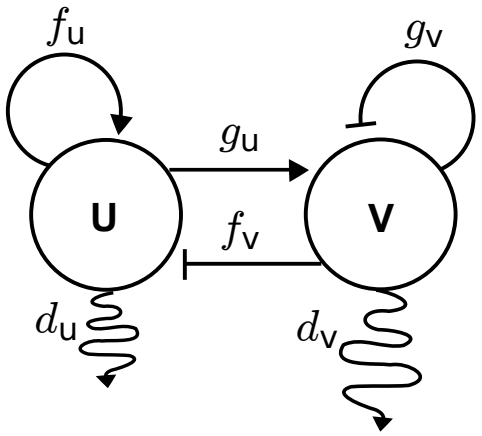

Figure S7: The network of the Activator-Inhibitor model

As an alternative, a Substrate-Depleted model could be obtained by inverting the signs of the parameter g_u and f_v. This would result in a model where an activator (u) depletes a substrate (v) to auto-activate itself. In this study we analyzed only the behavior of the Activator-Inhibitor model.

2.3 The effect of *Hox* genes

To investigate the possible role of Hox genes we analyzed how the different parameters of the model (Figure S7) affect the wavelength and the speed of pattern formation. To analyze the wavelength we first calculated the wavenumber k^2 of the mode with the largest eigenvalue λ as showed in [25]:

$$k^2 = \frac{-d_u d_v (f_u - g_v) + (d_u + d_v)\sqrt{-d_u d_v f_v g_u}}{d_u d_v (d_v - d_u)} \tag{4}$$

and calculated the wavelength ω of the corresponding one-dimensional case with zero-flux boundary conditions as presented in [43]:

$$\omega = \frac{2\pi}{\sqrt{k^2}} \tag{5}$$

To analyze the speed of appearance (λ_{max}) we use the formula presented in [25]:

$$\lambda_{max} = \frac{d_v f_u - d_u g_v - 2\sqrt{-d_u d_v f_v g_u}}{d_v - d_u} \tag{6}$$

The goal of our analysis was to identify which parameters can be modulated by Hox genes to increase both the wavelength ω and the speed of pattern formation

λ_{max}. Also we wanted to identify the parameters that defined the region where patterning mechanism was active, as we observed a progressive PD digit length reduction and no pattern was formed when *Hox* genes were completely removed. Formally, the pattern formation is achieved when the condition $\lambda_{max} > 0$ is satisfied.

Trivial candidates that could account for the increase in wavelength are the diffusion constants d_u and d_v. When we used the parameters presented in Table ST1 and allow only one of the diffusion constant to change at the time, d_u and d_v could vary in the following ranges according to (3):

$$d_u < 645.013 \quad d_v > 94.95$$

When d_u or d_v were increased as showed in Figure S8, the wavelength ω was increased.

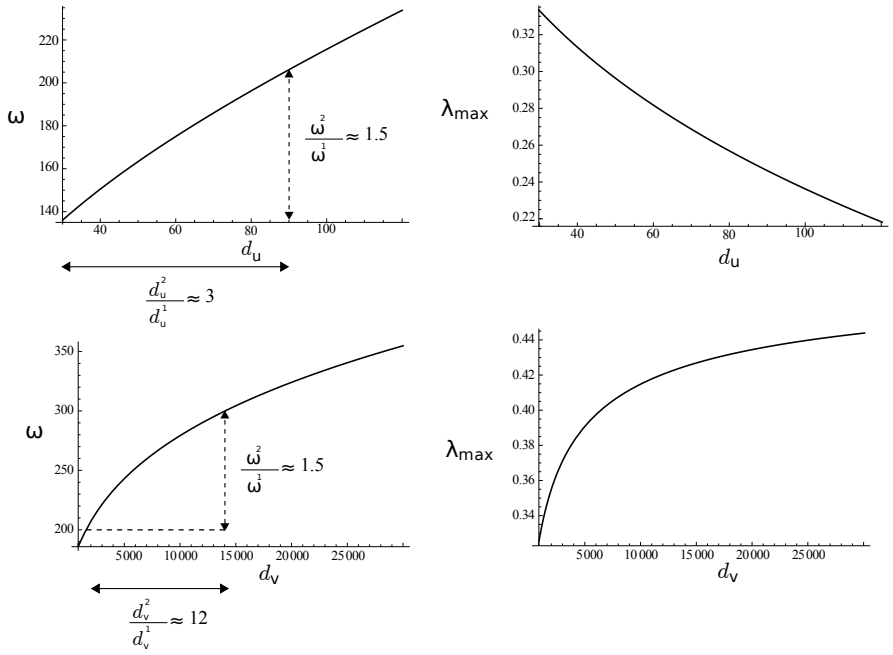

Figure S8: The effect of one diffusion constant on λ_{max} and ω

When the diffusion of the activator d_u was increased approximately three times the wavelength ω was increased of 1.5 times. In contrast, to obtain a similar increase in ω with the inhibitor, the diffusion constant d_v had to increase 12 times. Another difference between d_u and d_v was the relation with the speed of pattern appearance λ_{max}. In agreement with the results presented in [25], we

found that λ_{max} was decreased (slower pattern formation) when d_u increased while the opposite result occurred (faster pattern formation) when d_v increased. Therefore, assuming that Hox genes have to promote both faster pattern formation (greater λ_{max}) and bigger wavelength (greater ω) the only good candidate for being under the effect of Hox genes was d_v.

When we allowed both diffusion constants to vary at the same time, we could more easily obtain the desired change in ω by simultaneously scaling d_u and d_v of 1.5, as showed in Figure S9.

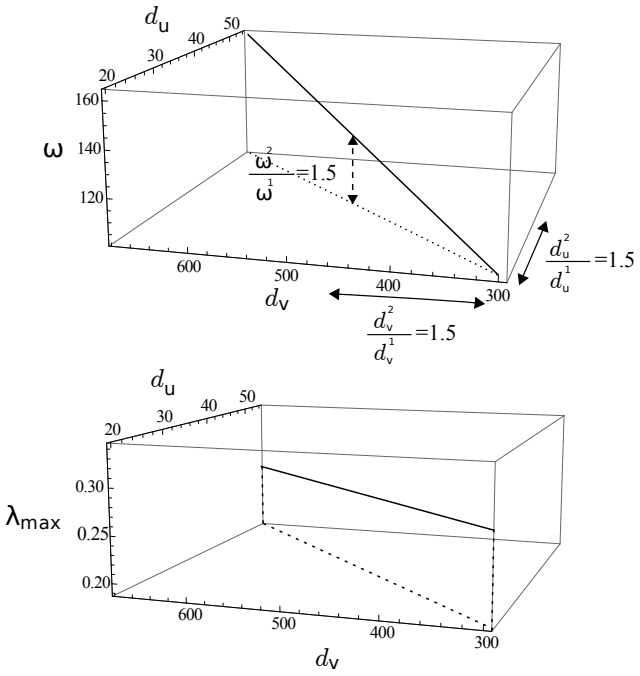

Figure S9: The effect of both diffusion constants on λ_{max} and ω

However, in this case λ_{max} remained constant.

In conclusion d_v was the only parameter that could account for both an increase in ω and λ_{max}. As mentioned above, d_v has to increase approximately 12 times to obtain the change in wavelength that we observe upon Hox genes removal. A recent study showed that similar differences in diffusion constants can indeed be observed in vivo [44]. It has been proposed that proteo-glycans in extracellular matrix can act as diffusion modulators [42]. However, the molecular basis of diffusion modulation remains largely unknown.

For this reason we concentrated our analysis on the reaction kinetic parameters f_u, f_v, g_u and g_v that are easier to relate to the change in gene regulation

that follows Hox alleles removal. We explicitly ignored more complex cases where reaction kinetic parameters were modulated in conjunction with diffusion constants. However, our analysis can be easily extended to consider the parameters d_v and d_u mentioned in the previous paragraph.

To analyze the effect of a change in the kinetic parameters, we allowed two parameters to change at the time and calculated the parameter region that respected the Turing-instability conditions (3). For each parameter couple we produced two graphs visualizing the Turing-instability region: one showed the change in wavelength ω and one showed the change in speed of pattern appearance λ_{max}. This allowed us to see the effect of a single parameter change in different regions and to investigate the relation between the parameters. In total we obtained 12 graphs (6 parameter couples), showed in Figure S4 and Figure S5. Our analysis of λ_{max} confirmed the results presented in [25] showing that an increase in the inhibition strength of f_v or in the activation strength of g_u decreases λ_{max} (slower pattern formation) while an increase in the activation strength f_u or in the inhibition strength g_v increases λ_{max} (faster pattern formation).

Our analysis of the wavelength ω instead revealed that an increase in strength of the auto-activation f_u or the the auto-inhibition g_v increases the wavelength while an increase in the cross-inhibition f_v and the cross-activation g_u decreases the wavelength. We also noted that across the parameter space, a change in f_v or in g_u has a greater effect on the wavelength than a change in f_u or in g_v. In particular we found that f_v and g_u were the only parameters able to produce enough change in wavelength to account for the reduction observed upon Hox removal.

In conclusion either a decrease in the activation strength of g_u or a decrease in the inhibition strength f_v was able to reliably promote enough increase in ω and in λ_{max}. This may depend on the specific difference d_u and d_v that we choose and it may change if we consider more complex Turing models with basal productions or non-linear terms. However, within the scope of this analysis f_v and g_u were the best candidates for being under the control of Hox genes.

2.4 Numerical Simulations

Next, we performed a number of two-dimensional numerical simulations to explore the effect of the different parameters on the pattern. This requires integrating partial differential equation of the form (1). To this extent, we developed our own numerical simulator that integrates the reaction part using a second order Runge-Kutta method with adaptive time-step (also known as Heun's method) and a Finite Volume Method to solve the diffusion part. The Heun method estimates an error by comparing the results obtained with an Euler Method with the results obtained with a second order Runge-Kutta. According to this error, the time-step is resized during the simulation. The Finite Volume Method simulates the diffusion between neighboring triangles on an unstructured triangular grid. This is obtained by applying the Fick's law of diffusion on each edge of the grid to diffuse the reactants between triangle centroids.

All the simulations that we performed had zero-flux boundary conditions for the diffusible species. The initial conditions were obtained with a random Gaussian perturbation around the homogeneous steady state $(u, v) = (0, 0)$ with magnitude of the order 10^{-3}. Moreover, to make sure that our results were robust against noise we added a 1% of multiplicative Gaussian noise to both u and v throughout the simulation. The simulations were run until a stable pattern was reached.

To explore the two-dimensional patterns that were formed by this system, we initially generated a square grid using the finite element grid generator Gmesh [38]. The triangular grid is shown in Figure S10.

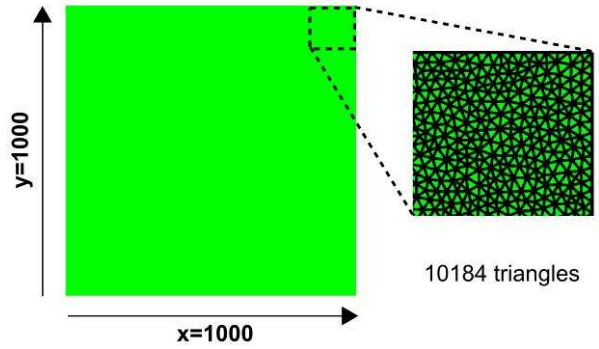

Figure S10: The square triangular grid used for the numerical simulations

Simulations on the square domain revealed that this general Turing model always produces stripes due to the reverse symmetry of the system given by the u^3 term. This was a suitable feature to produce digit-like patterns. However, quadratic terms could be introduced in the reaction part to produce a spot like pattern. Next, we investigated how the speed of pattern appearance (λ_{max}) affects the pattern that is formed. This was done by running simulations with different values of f_u, as this parameter is mostly affecting λ_{max} and is virtually not changing ω. We found that for low values of λ_{max} the stripes directionality was quite homogeneous across the domain, while for high values of λ_{max} irregular labyrinth-like patterns were formed. This is highlighted in Figure S11.

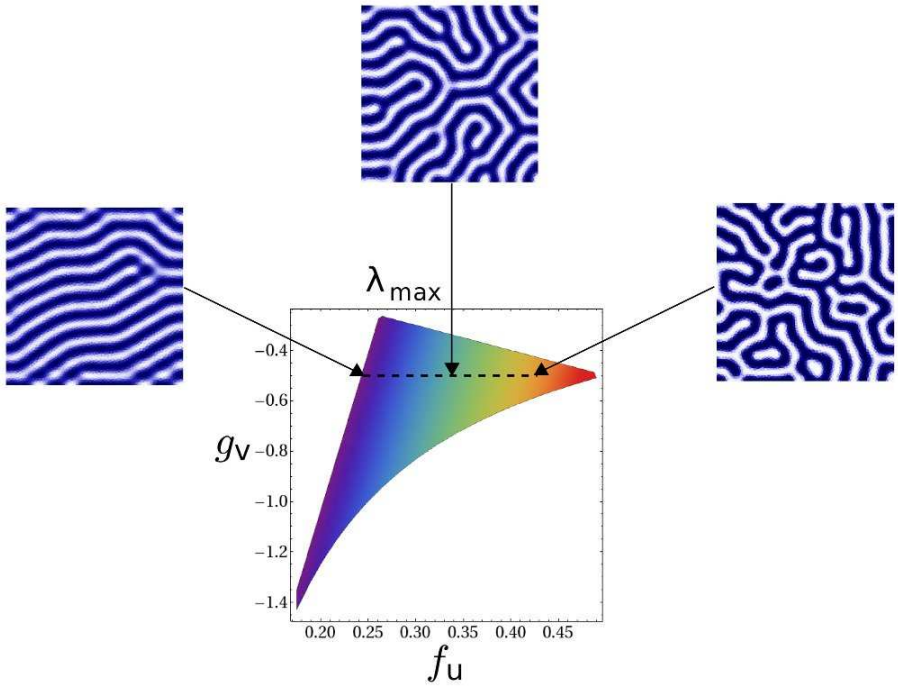

Figure S11: The effect of λ_{max} on stripe directionality

Related findings have been recently presented in [45]. However, even for small λ_{max} the overall directionality of the stripes was random. Stripe directionality is a crucial aspect to obtain a robust pattern formation in real biological systems. It has been showed that stripe orientation can be controlled with anisotropic diffusion [46] or with specific boundary conditions [36]. Since there is no evidence for either of these two features in the limb bud, we searched for an alternative strategy.

Interestingly, we found that under certain conditions a spatial gradient of λ_{max} is able to orient the stripes. This is shown in Figure S12 where f_u was scaled along the x axis with an exponential function.

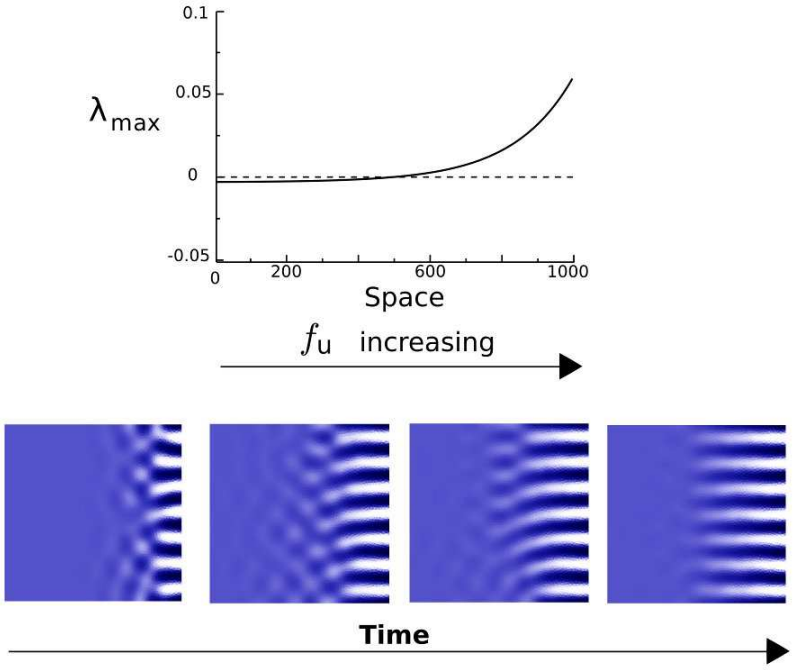

Figure S12: Stripe orientation with f_u spatial scaling

Intuitively, stripe orientation is achieved because the pattern forms earlier in the regions with a high λ_{max} and subsequently propagates in the regions with smaller λ_{max}. Because of the exponential gradient, the region where the pattern is initially formed is quite narrow and a regular aligned pattern can be obtained. We found that this mechanism worked independently from the initial conditions, was robust to noise and was able to orient stripes with different wavelengths. Depending on the range of f_u that was considered, different gradients had to be used to obtain a good orientation. Moreover, we found that the orientation was better when very high values of λ_{max} were avoided. However, we consistently found that exponential gradients or short linear gradients were able to drive stripe orientation. In contrast, a gradient with a logarithmic profile promoted almost the opposite alignment (parallel to the gradient) .

We hypothesized that this strategy is used in the limb to orient the digits toward the distal tip. This implies that a distal gradient (e.g. Fgfs coming from the Apical Ectodermal Ridge - AER) has to increase f_u and therefore λ_{max} to orient the stripes. Interestingly, this hypothesis is consistent with the results presented in [25] that show that Fgfs increase λ_{max} in micromass culture. It is therefore plausible that Fgfs in combination with growth are indeed helping to

get the correct digit alignment in vivo.

Next we performed numerical simulations on a domain with the experimental shape of the *Gli3* -/- mutant. We used an outline of a representative specimen and generated a triangular grid with the software Gmesh. The resulting triangular grid is shown in Figure S13.

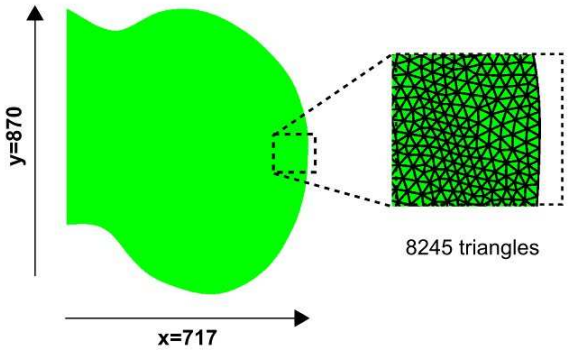

Figure S13: The triangular limb grid made from the experimental *Gli3* -/- shape

We mapped the experimental expression pattern of *Hoxa13* into this realistic domain shape by using the Vtk library [35]. Eventually, we normalized the expression pattern between 0 and 1. This expression pattern was used as an approximation for *Hox* genes in the model. In addition, we simulated an Fgf signaling gradient by diffusing a substance from a region corresponding to the AER into the mesenchyme. The patterns of *Hox* expression and Fgf signaling are showed in Figure S14.

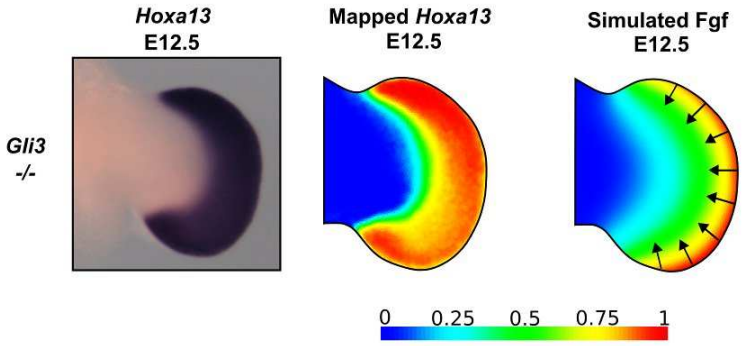

Figure S14: The patterns of *Hox* expression and Fgf signaling

The Fgf gradient was simulated with the following equation:

$$\frac{\partial Fgf}{\partial t} = \alpha_{fgf} - \mu_{fgf} Fgf + d_{fgf} \nabla^2 Ffg$$

with parameters:

$$\alpha_{fgf} = 1, \quad \mu_{fgf} = 0.01, \quad d_{fgf} = 400$$

where α_{fgf} is a source term that was active only on the distal boundary that corresponds to the AER (highlighted by the arrows in Figure S14). In the rest of the domain zero-flux boundary conditions were used. Eventually, the gradient was normalized between 0 and 1.

The two PD profiles of Fgf and *Hox* are shown in Figure S15.

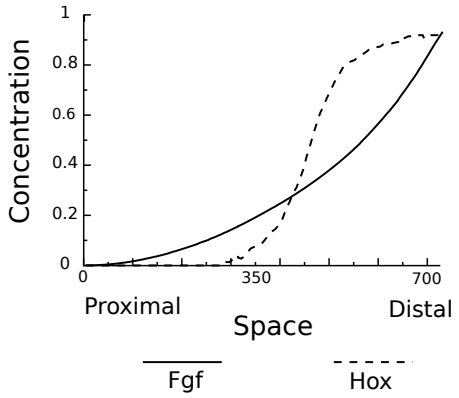

Figure S15: The PD profiles of Fgf and *Hox*

2.5 Details of the Simulations in Fig 1D-E

The concept of modulating Turing parameters in a non-homogeneous manner, using global gradients, has previously been explored in 1D [41] and more recently in 2D [39]. Here, to test the hypothesis that a PD graded modulation of the wavelength was required to avoid digit bifurcations, we explored the effect of a uniform and a graded PD distribution of the parameters that we identified as the best candidates to modulate the wavelength: f_v and g_u. We developed a model where f_v and g_u were either constant or modulated by Fgf within an active distal region. The active distal region was defined by using the following equations:

$$f(u,v) = (f_u + k_{fu} \cdot Fgf)u + f_v v - u^3$$
$$g(u,v) = g_u u + g_v v \tag{7}$$

This strategy provided a gradient of f_u that promoted correct stripe orientation. Moreover, by starting from f_u values that were outside the Turing-instability region and by choosing an appropriate value for k_{fu} we were able to define an active distal region that reflected the PD size of the *Gli3 -/-* digital region. This was done by calculating λ_{max} along the PD axis and by comparing the region were $\lambda_{max} > 0$ (active patterning) with the digit PD length of the *Gli3 -/-* mutant.

Using this model we then explored the effect of a uniform and a graded distribution of f_v and g_u.

2.5.1 Figure 1D - Uniform wavelength distribution

In this case we set f_v and g_u to constant values. In addition, we selected an appropriate range for f_u to obtain correct stripe orientation. We selected values of f_v and g_u to match to the average wavelength of the *Gli3 -/-* mutant. Simulations with a uniform value of f_v and g_u showed distal digit bifurcations that were due to the bigger distal autopod size. The simulation showed in Figure 1D of the main text was obtained with the parameter set showed in table ST1 except for the following parameters:

$$f_u = 0.28, \quad k_{fu} = 0.15; \quad g_u = 0.75$$

This parameter set is represented graphically in Figure S16.

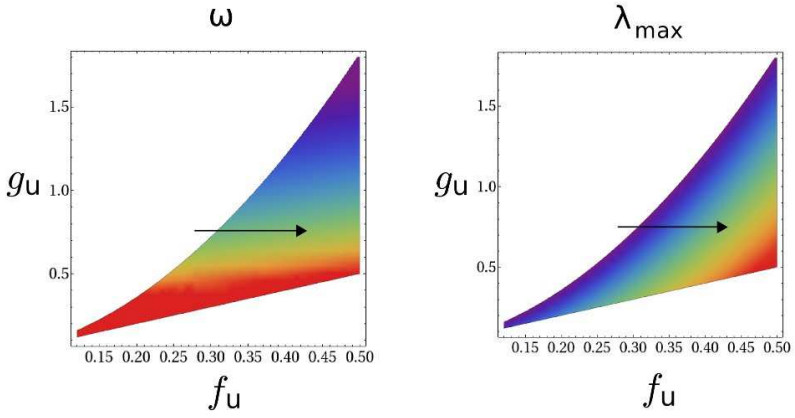

Figure S16: Graphical representation of the parameters used in the simulation of Figure 1D

The black arrow represents the parameter values seen along the PD axis of the domain. It shows the change in f_u that is promoted by Fgf to drive the stripe orientation. The arrow starts from a parameter region where there is no Turing-instability (white region) and ends up in an active region (colored region) where $\lambda_{max} > 0$ and a pattern is formed. Since f_u is changed by Fgf (a proximal-distal graded signal) a distal active region is obtained. λ_{max} and ω along the PD autopod profile are shown in Figure S17.

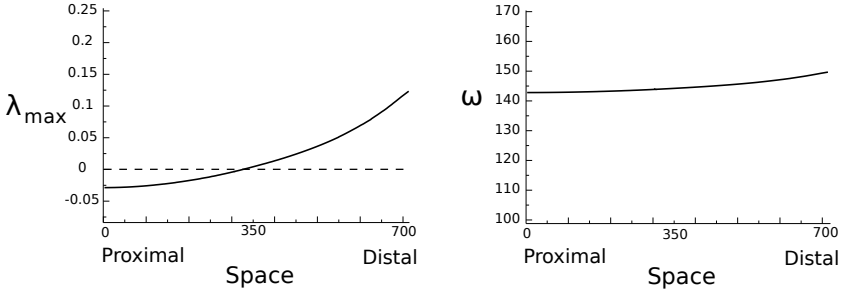

Figure S17: λ_{max} and ω PD profiles of the simulation in Figure 1D

The graph on the left shows λ_{max}. The region above the dashed line (λ_{max}=0) is the active distal region. The graph on the right highlights the uniform wavelength distribution obtained with a constant f_v and g_u. The slight increase in wavelength in the distal part of the limb is due the increase in f_u that was used to align the stripes. However, it was found to be negligible with respect to the pattern formed.

2.5.2 Figure 1E - PD Graded wavelength

In this case we modulated the wavelength by changing either f_v or g_u with the Fgf gradient. Similarly to the previous case we also selected an appropriate range for f_u to obtain correct stripe orientation.

First we simulated a change in the parameter f_v. To this extent we modified the equations (7) in the following way:

$$f(u,v) = (f_u + k_{fu} \cdot Fgf)u + (f_v + k_{fv} \cdot Fgf)v - u^3$$

the equation $g(u,v)$ was unchanged. We chose parameters f_u, f_v, k_{fu}, k_{fv} that started from a parameter region where $\lambda_{max} < 0$ and moved towards a parameter region where ω was increased. A graphical example of the parameters that we used is showed in Figure S18.

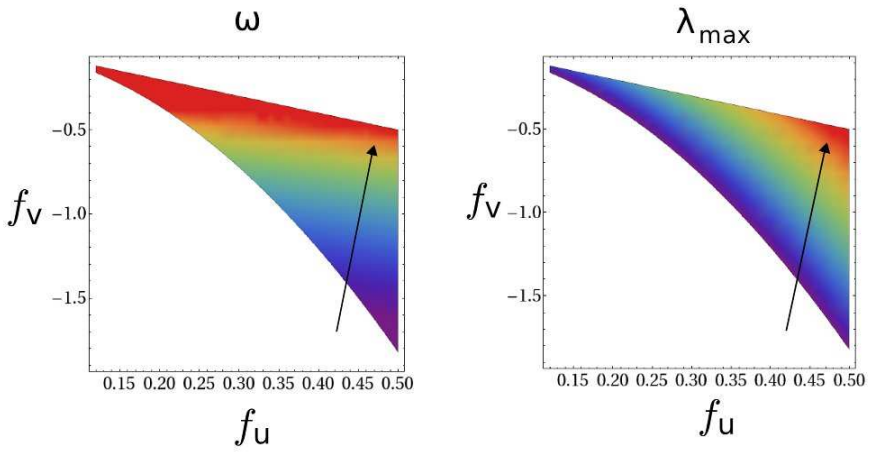

Figure S18: Graphical representation of the parameters used in the PD graded f_v case

The arrow highlights the change in f_v and f_u that is promoted by Fgf. The starting point of the arrow is outside the Turing-instability region (white region) where $\lambda_{max} < 0$. The specific arrow presented above was obtained with the following parameters:

$$f_u = 0.42, \quad k_{fu} = 0.05, \quad f_v = -1.7, \quad k_{fv} = 1.1$$

Unfortunately, we found consistently that the stripe orientation was compromised. In particular, the pattern traveled toward the distal tip of the limb and in this way the orientation provided by f_u was disrupted. An example of the qualitative behavior that we observed is shown in Figure S19.

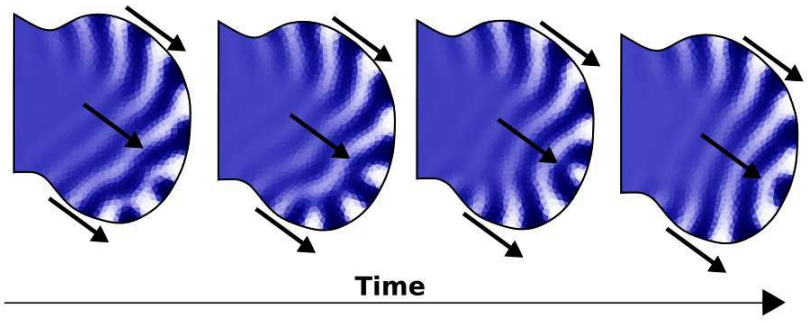

Figure S19: Example of simulation with a PD graded f_v

The arrows highlight the direction where the pattern was moving over time. We tried different combinations of Fgf gradients and different f_v and f_u ranges but found consistently that this behavior was difficult to avoid. Intuitively, this was happening because a lower strength of f_v in the distal tip destabilized the activator pattern and produced the traveling behavior. Therefore, with our current alignment strategy, we could not manage to modulate f_v to match the skeletal pattern of the *Gli3 -/-* mutant.

We decided to discard this strategy and try with the parameter g_u. This time we modified the equation (7) in the following way:

$$\begin{aligned} f(u,v) &= (f_u + k_{fu} \cdot Fgf)u + f_v v - u^3 \\ g(u,v) &= (g_u - k_{gu} \cdot Fgf)u + g_v v \end{aligned} \tag{8}$$

Like in the previous case, we chose a parameter set f_u, g_u, k_{fu}, k_{gu} that started from a region where $\lambda_{max} < 0$ and moved towards a parameter region where the ω was increased. This time our simulations revealed that the orientation of the stripes was not compromised. Indeed, we consistently found that a PD graded g_u was actually helping to get a good orientation. The simulation showed in Figure 1E was obtained with the parameter set showed in Table ST1 except for the following parameters:

$$f_u = 0.42, \quad k_{fu} = 0.05, \quad g_u = 1.7, \quad k_{gu} = 1.1$$

A graphical representation of the parameters that were used is shown in Figure S20.

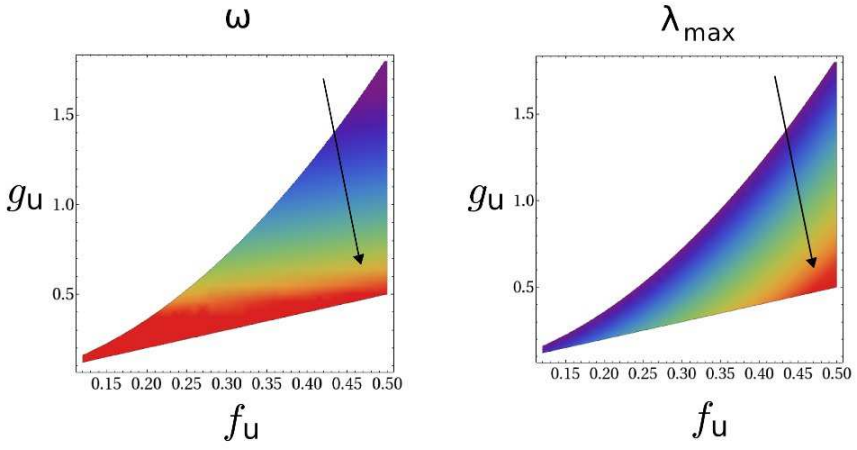

Figure S20: Graphical representation of the parameters used in the simulation of Figure 1E

Like in the previous case, the arrow represented the PD change in g_u and f_u that was promoted by Fgf. λ_{max} and ω along the a PD autopod profile are shown in Figure S21.

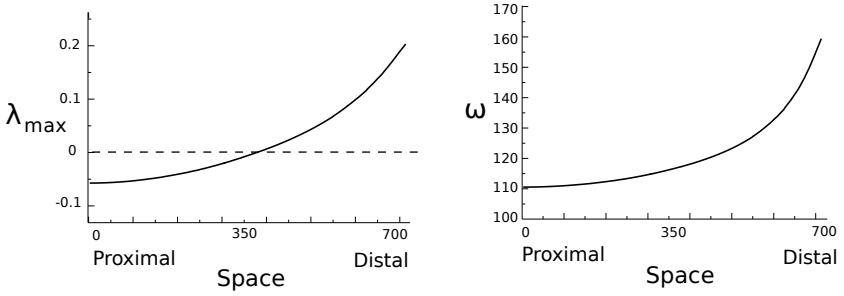

Figure S21: λ_{max} and ω PD profiles of the simulation in Figure 1E

The graded wavelength prevented distal digit bifurcations and helped to obtain the correct orientation of the stripes. This highlighted that an effective PD scaling of the wavelength was required if digit bifurcations had to be avoided. In conclusion, our quantification provided evidence that distal *Hox* genes modulated the wavelength. Moreover, we found both from the quantification and from our computational analysis that this modulation has to be done in a PD graded manner to avoid distal digit bifurcation. Therefore, in our model we assumed that *Hox* genes modulate the wavelength in a PD graded manner by cooperating with AER secreted molecule like Fgfs.

2.6 Details of the Simulations in Fig 3

To simulate the effect of the Hox gene alleles removal, we extended the model that had a PD graded g_u to consider Hox genes. We modified the equations (8) in the following way:

$$g(u,v) = (g_u - k_{gu} \cdot \boldsymbol{k_{hox}} Hox \cdot Fgf)u + g_v v$$

$f(u,v)$ was unchanged. The new *Hox* term corresponded to the experimental pattern of *Hoxa13* that we mapped into the grid. The parameter $\boldsymbol{k_{hox}}$ was a weight constant that represented the *Hox* dose and that was initially set to 1. We left the scaling of the parameter f_u in the model that promoted correct

stripe orientation. The network diagram of the model is highlighted in Figure 4A of the main text.

First, we chose parameters that were able to match the skeletal pattern of *Gli3 -/-* mutant and its wavelength distribution along the PD axis (black line Figure 4B). The same parameters that we used for the simple PD graded g_u model were found to be still suitable to match the *Gli3 -/-* pattern. The parameters were those presented in table ST1 except for the following parameters:

$$f_u = 0.42, \quad k_{fu} = 0.05, \quad g_u = 1.7, \quad k_{gu} = 1.1$$

This parameter set is highlighted by the read arrow in Figure S22.

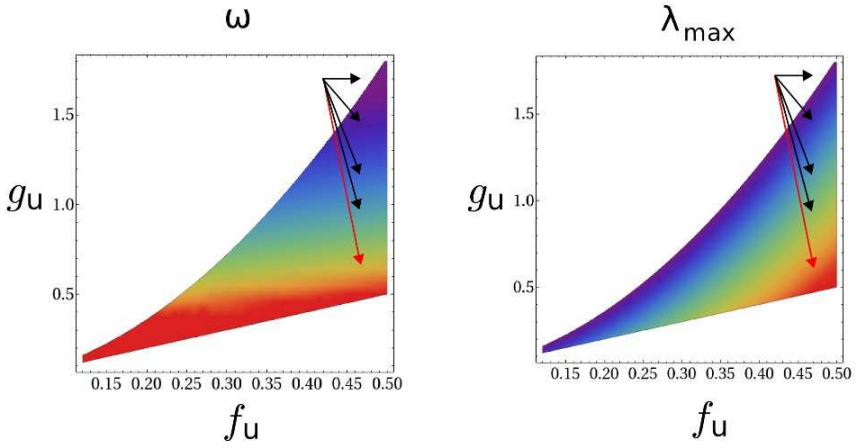

Figure S22: Graphical representation of the parameters used in the simulations of Figure 3

We simulated the progressive removal of *Hox* alleles by decreasing the parameter $\boldsymbol{k_{hox}}$ that represented *Hox* dose. This is shown by the progressively shorter black arrows in Figure S22. When *Hox* dose was reduced, ω (wavelength) and λ_{max} (patterning speed) were decreased. Moreover, the wavelength PD scaling became shallower and distal digit bifurcations occurred. In addition, the size of the active patterning region, that defined the PD digit length, was also reduced. This is highlighted in Figure S22 by the fact that a progressively shorter proportion of the black arrows is overlapping with the Turing-instability region where $\lambda_{max} > 0$ (colored region). All these behaviors were consistent with the phenotypes observed upon *Hox* alleles removal. Figure S6 shows how ω and λ_{max} changed along a PD axis of the autopod when *Hox* dose was reduced, all the features discussed above are highlighted graphically.

The values of $\boldsymbol{k_{hox}}$ that were used to simulate the progressive *Hox* dose reduction are shown ST2.

$Hoxa13$ $Hoxd11-13$	$+/+$ $+/+$	$+/-$ $+/-$	$+/+$ $-/-$	$+/-$ $-/-$	$-/-$ $-/-$
k_{hox}	1	0.7	0.5	0.2	0

Table ST2: Values of k_{hox} used in the simulations of Figure 3

3 Supplementary Material for Figure 1C

3.1 Wavelength quantification of the WT

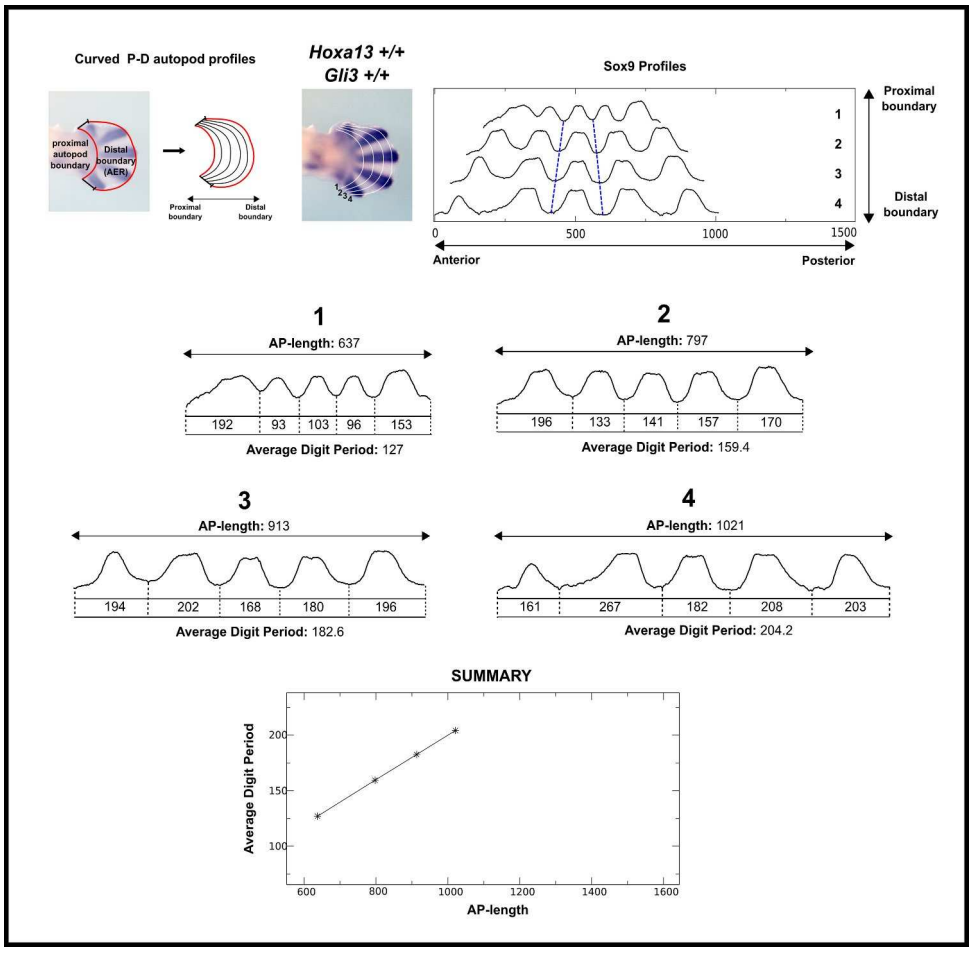

3.2 Wavelength quantification of the *Gli3 -/- ; Hoxa13 +/+* mutant

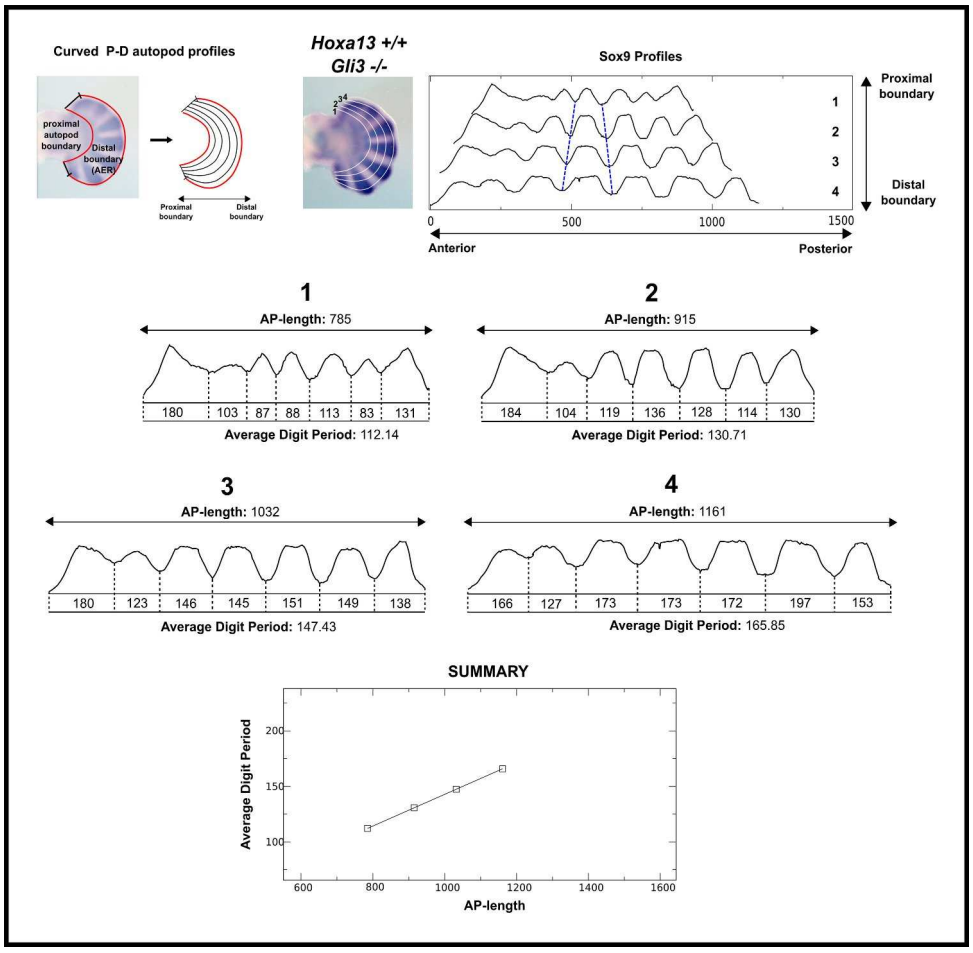

3.3 Wavelength quantification of the *Gli3 -/- ; Hoxa13 +/-* mutant

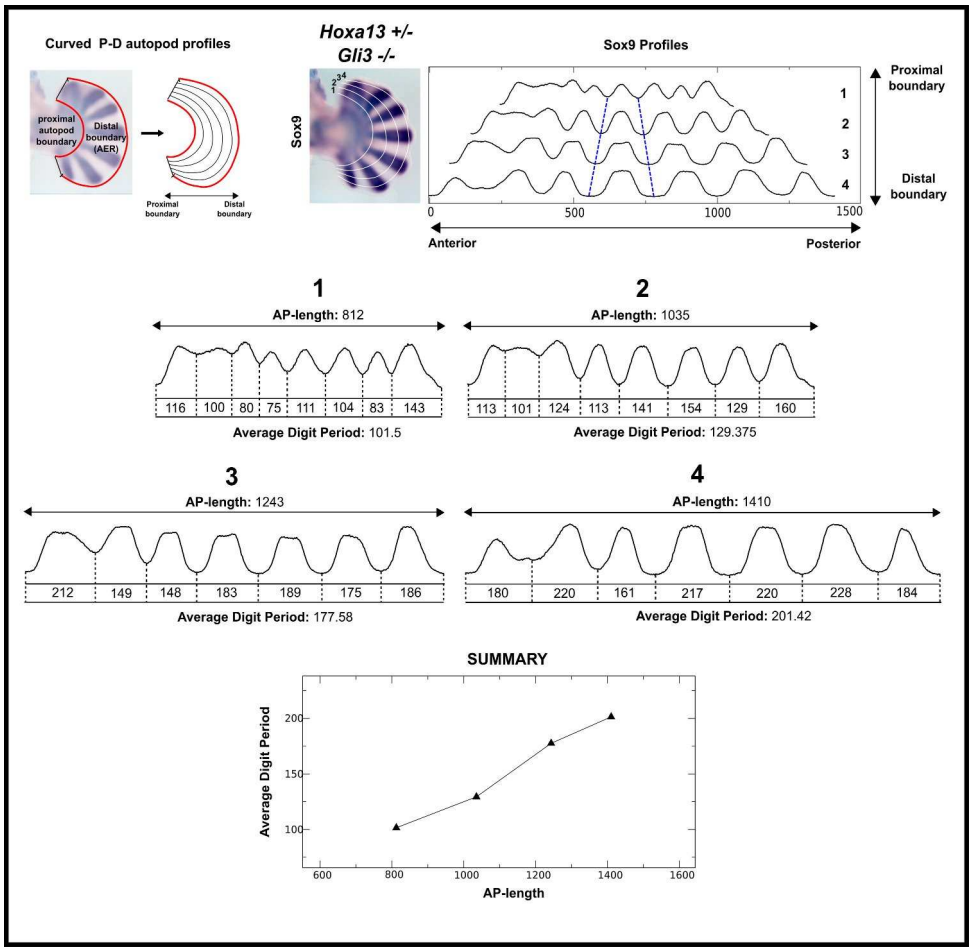

3.4 Wavelength quantification of the *Gli3 -/- ; Hoxa13 -/-* mutant

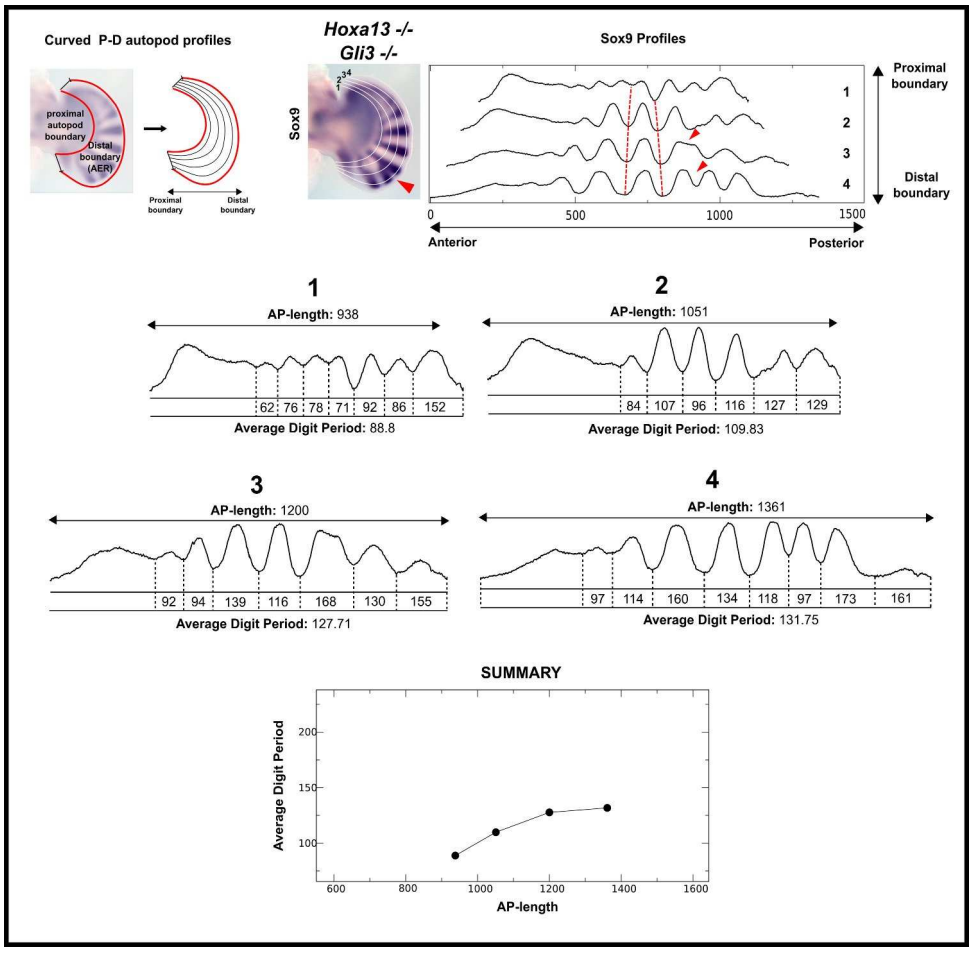

4 Supplementary Material for Figure 4B

4.1 Wavelength quantification of the *Gli3 -/- ; Hoxa13 +/+; Hoxd11-13 +/+* mutant

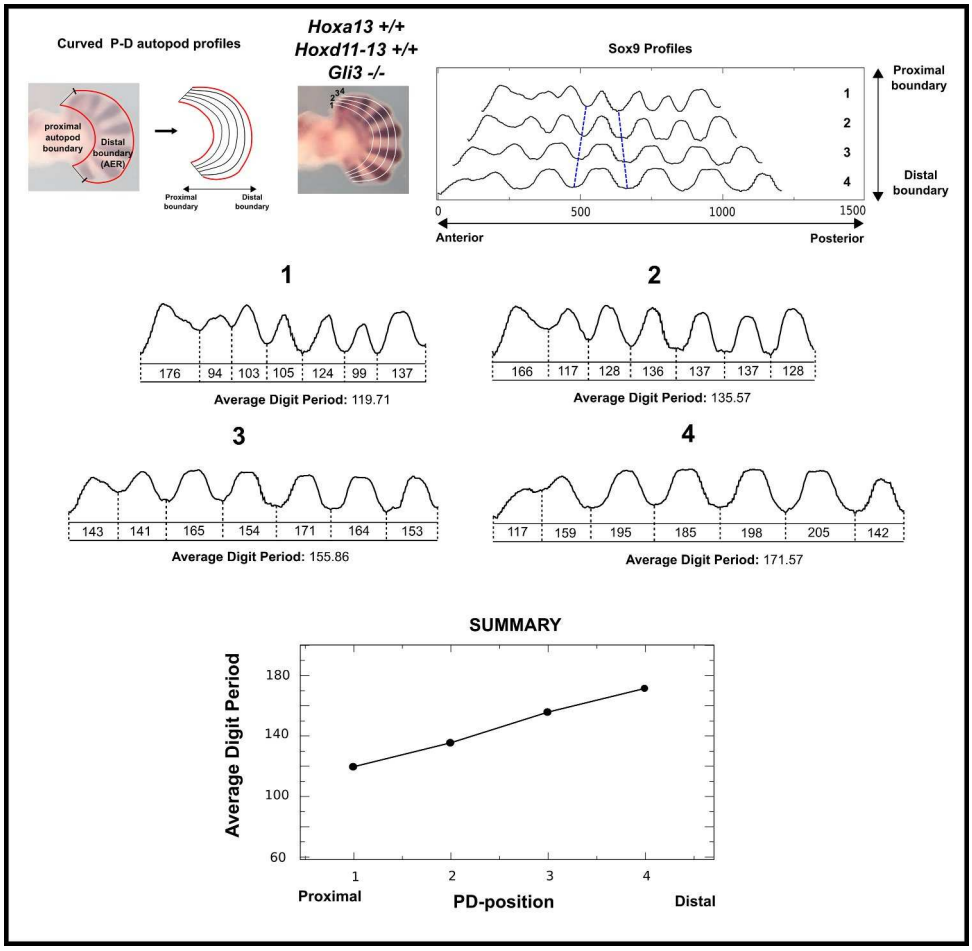

4.2 Wavelength quantification of the *Gli3 -/- ; Hoxa13 +/-; Hoxd11-13 +/-* mutant

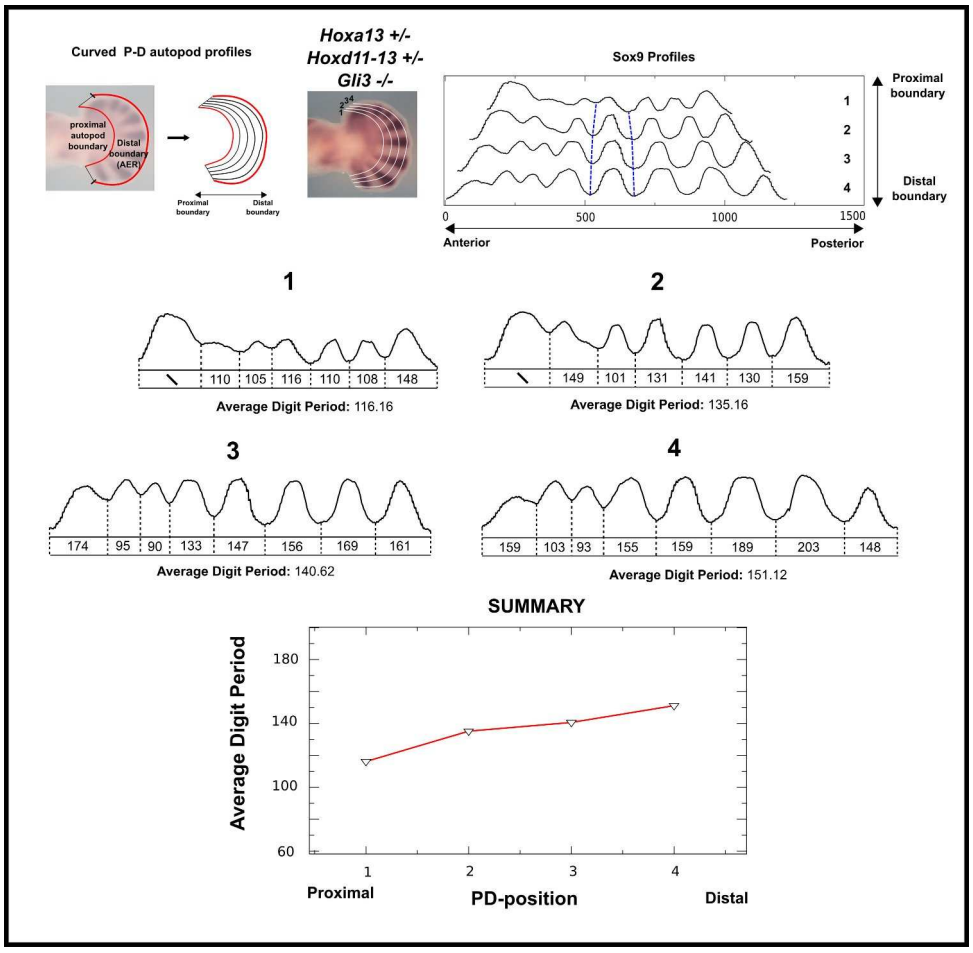

4.3 Wavelength quantification of the *Gli3 -/- ; Hoxa13 +/+; Hoxd11-13 -/-* mutant

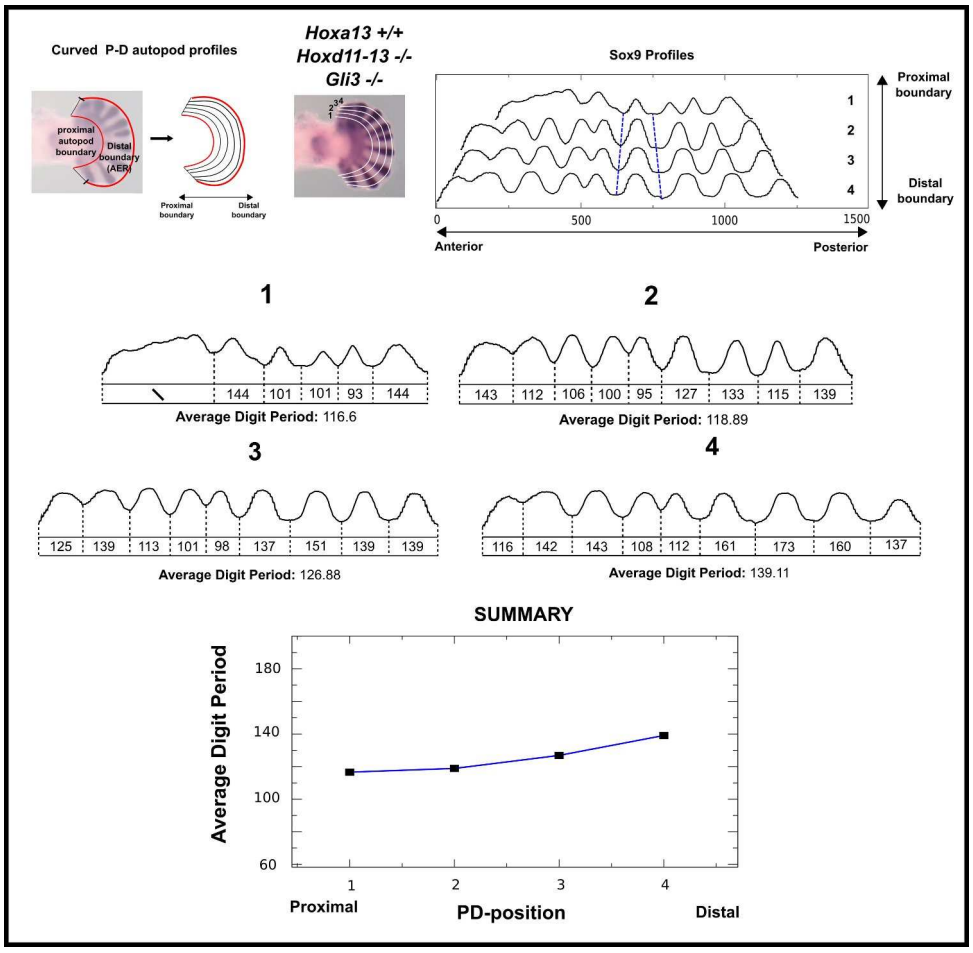

4.4 Wavelength quantification of the *Gli3 -/- ; Hoxa13 +/-; Hoxd11-13 -/-* mutant

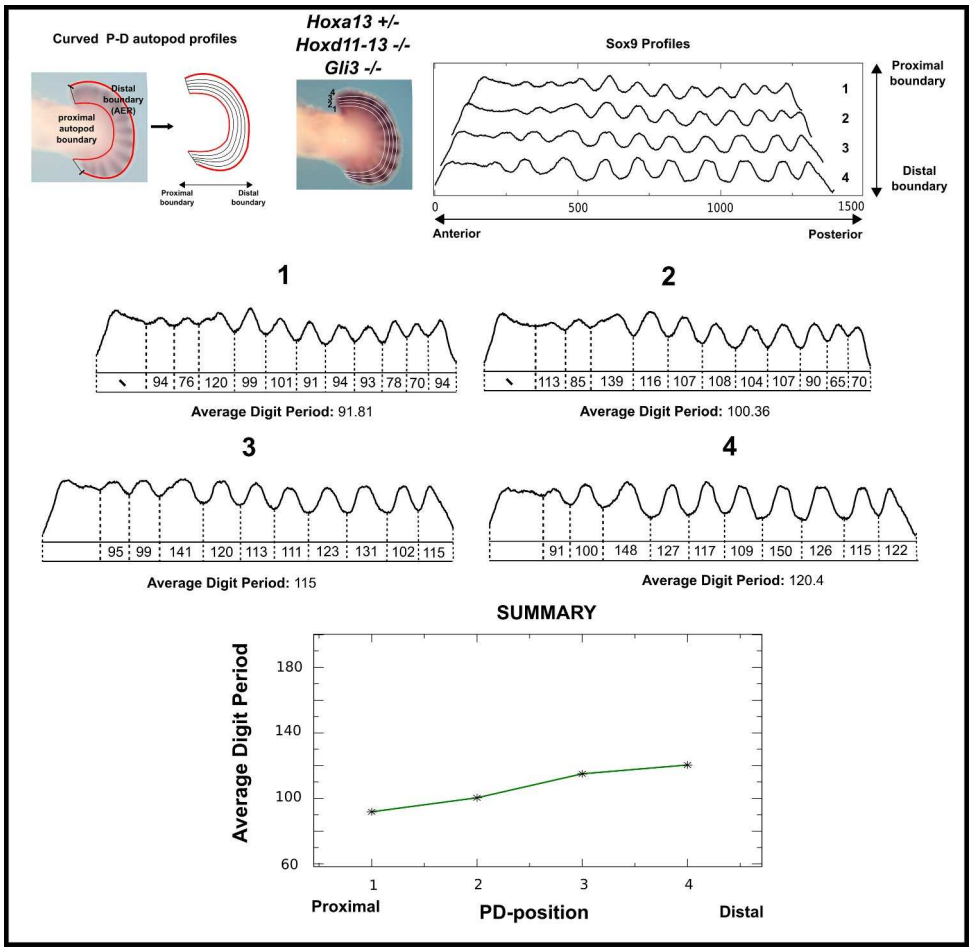

5 Supplementary Material for Figure 4C

5.1 Average wavelength quantification of the *Gli3* +/+ background mutants

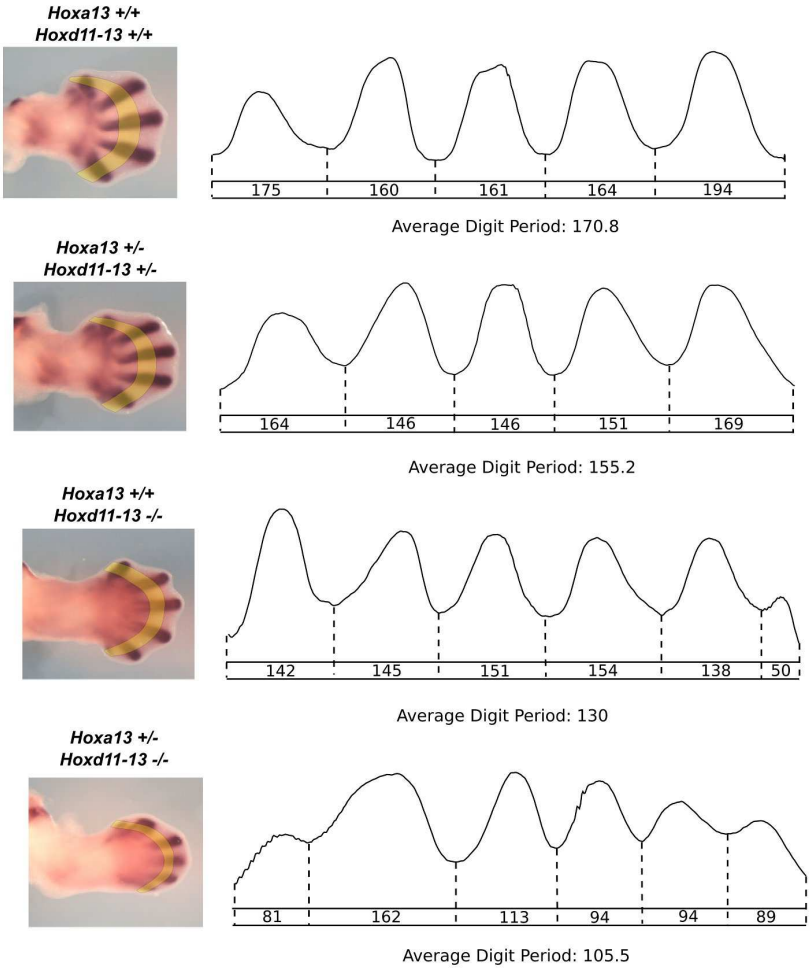

5.2 Average wavelength quantification of the *Gli3* +/- background mutants

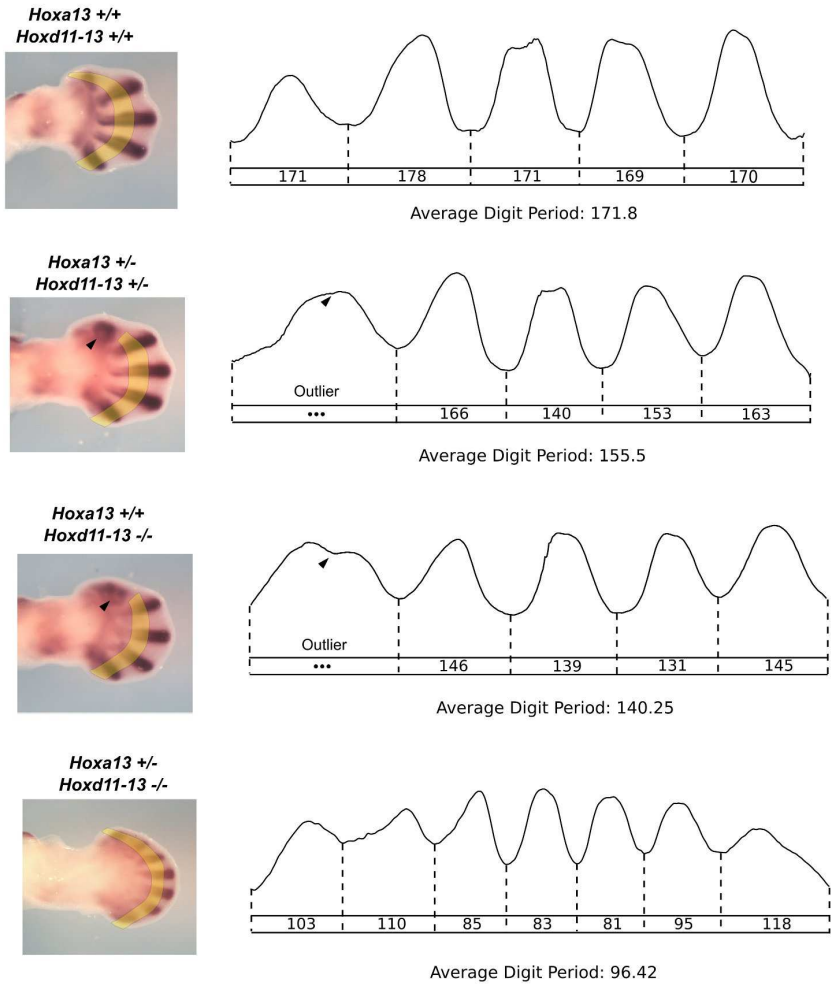

5.3 Average wavelength quantification of the *Gli3* -/- background mutants

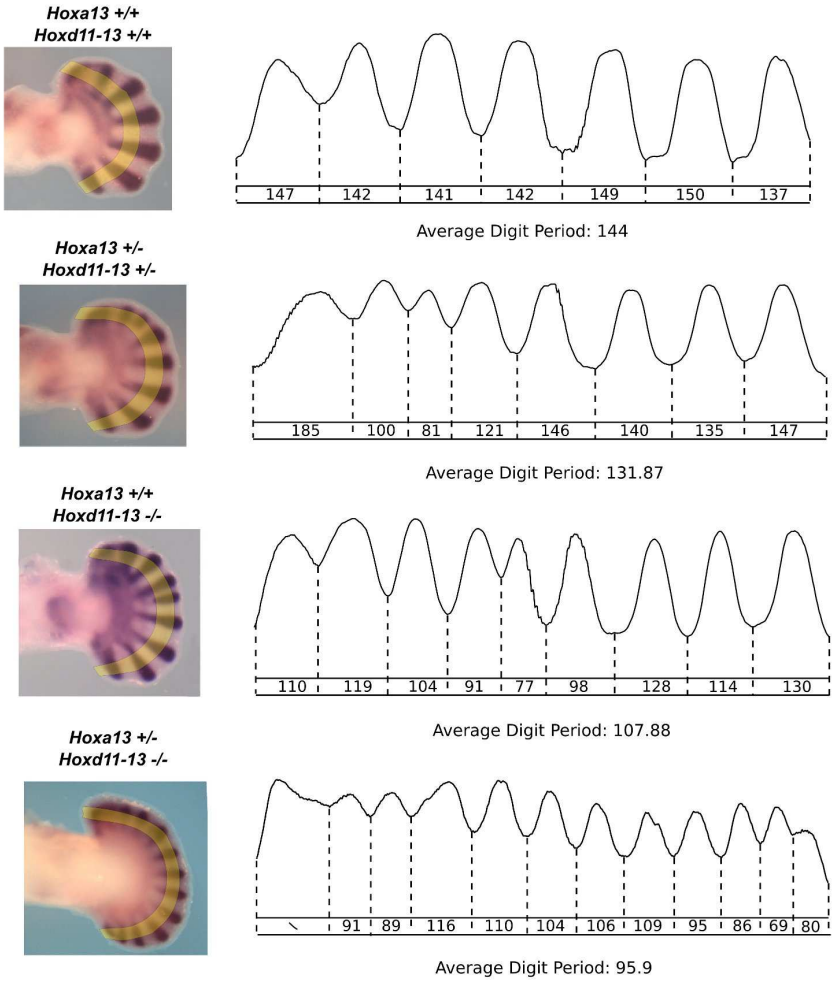

6 Figure S1

Expression of *Hoxd13* and *Hoxd12* in E12.5 limbs of the *Hoxa13;Gli3* allelic series. Note anterior upregulation of *Hoxd13* and *Hoxd12* in absence of *Gli3*. Genotypes are marked at the top of each column and probes on the left.

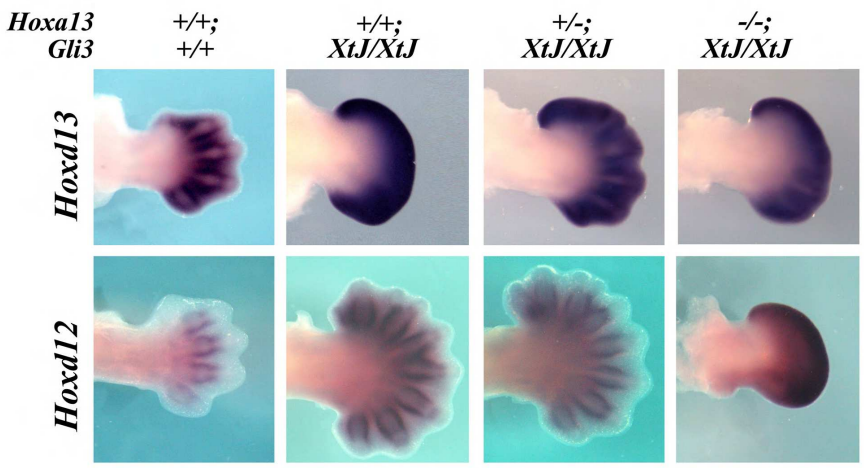

7 Figure S2

Expression of *Sox9* in limbs of the *Hoxa13;Hoxd11-13;Gli3* allelic series. Note the delay in the formation of the digit pattern when the *Hox* dose is low (*Hoxa13+/-;Hoxd11-13-/-*).

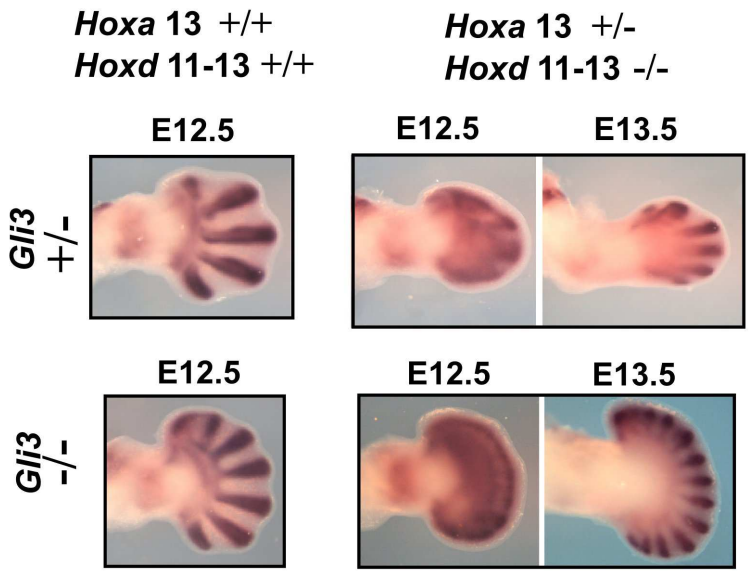

8 Figure S3

Expression of *Coll21a* in E14.5 limbs of the *Gli3*-null background with progressive decrease in distal *Hox* dose showing the reduction in the PD extension of the digital region.

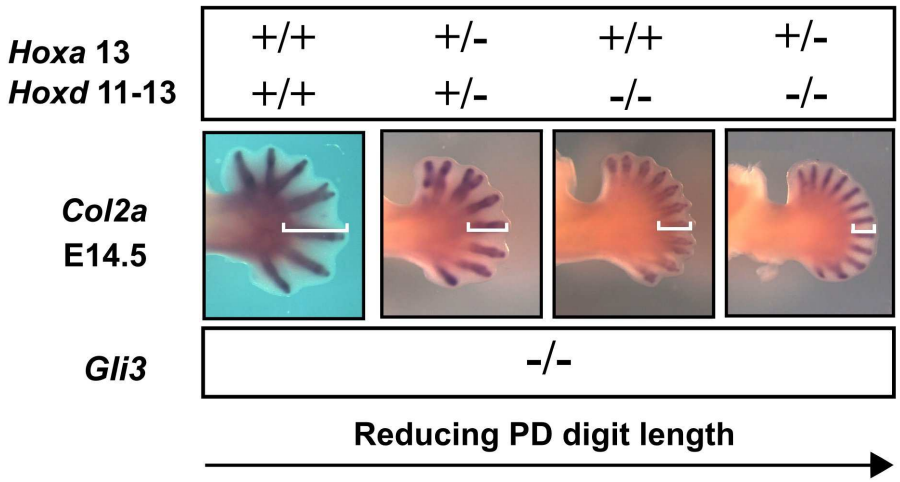

9 Figure S4

The effect of the reaction parameters on λ_{max} and ω: (f_u, f_v),(f_u, g_u) and (f_v, g_u). Two graphs visualizing the change in speed of pattern appearance (λ_{max}) and wavelength (ω) within the Turing-instability region are shown for each parameter couple.

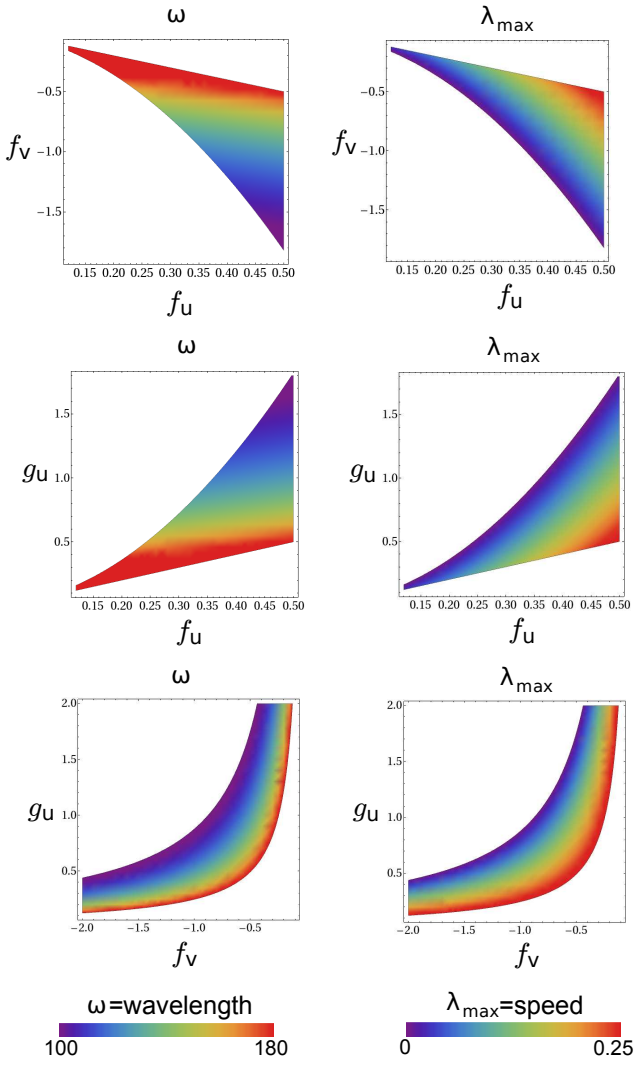

10 Figure S5

The effect of the reaction parameters on λ_{max} and ω: (f_u, g_v),(g_v, f_v) and (g_u, g_v). Two graphs visualizing the change in speed of pattern appearance (λ_{max}) and wavelength (ω) within the Turing-instability region are shown for each parameter couple.

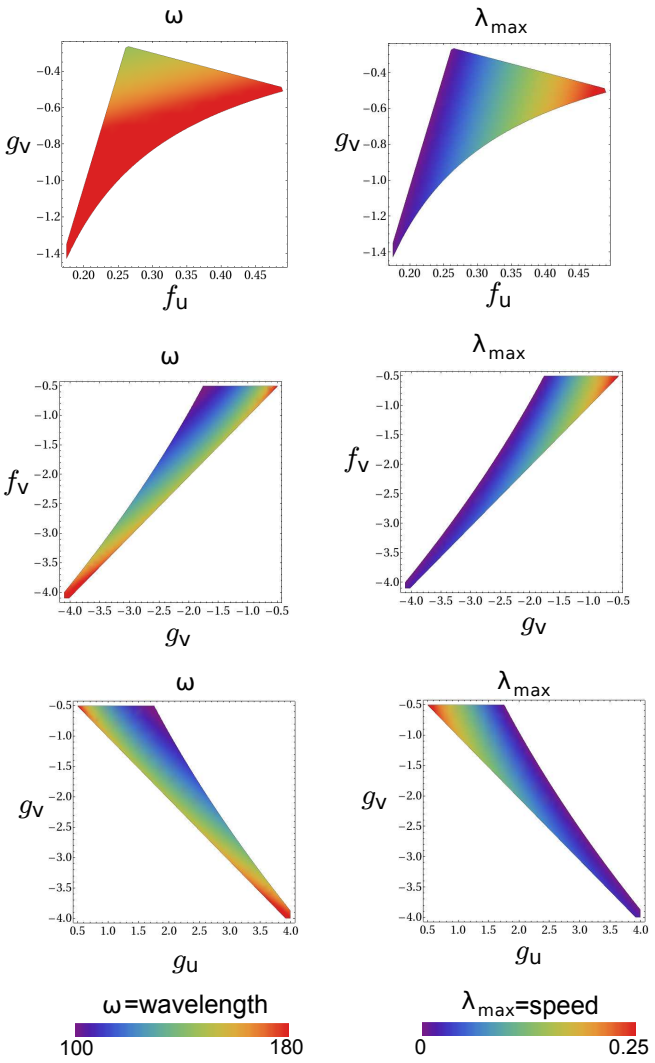

11 Figure S6

λ_{max} and ω PD profiles of the simulation in Figure 3

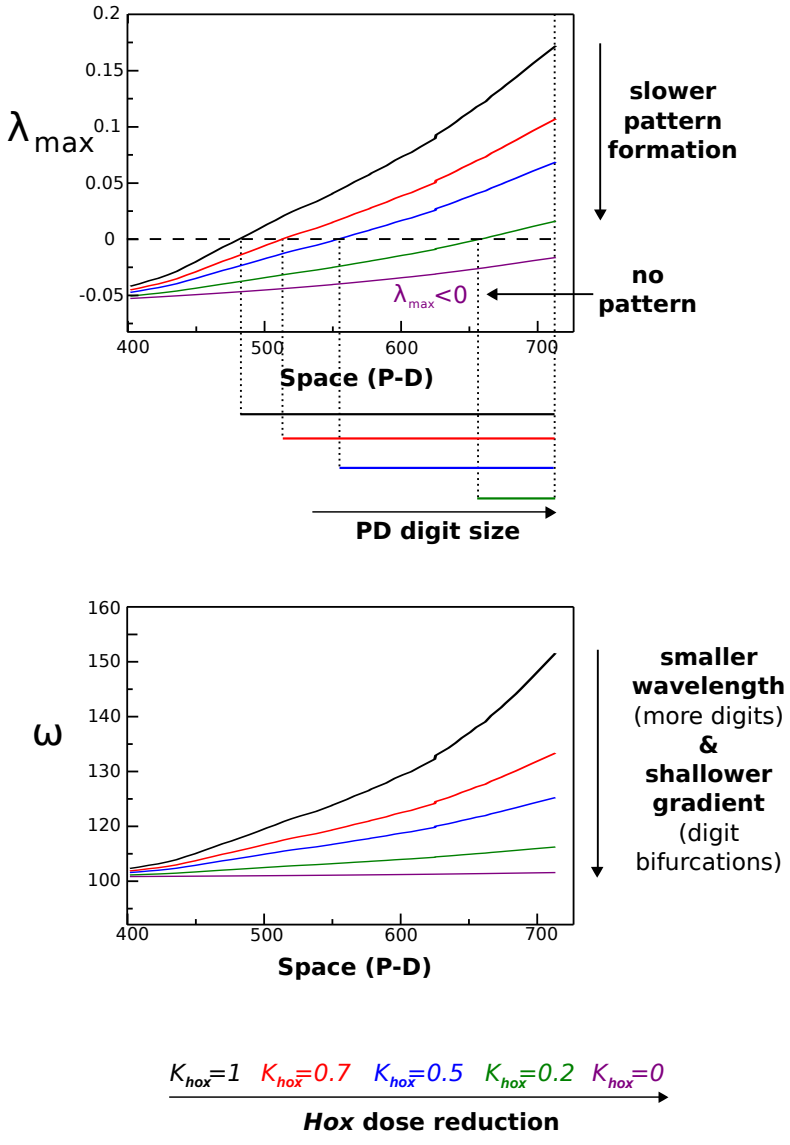

References and Notes

1. M. F. Bastida, M. A. Ros, How do we get a perfect complement of digits? *Curr. Opin. Genet. Dev.* **18**, 374 (2008). doi:10.1016/j.gde.2008.06.009 Medline

2. R. Zeller, J. López-Ríos, A. Zuniga, Vertebrate limb bud development: Moving towards integrative analysis of organogenesis. *Nat. Rev. Genet.* **10**, 845 (2009). doi:10.1038/nrg2681 Medline

3. B. Wang, J. F. Fallon, P. A. Beachy, Hedgehog-regulated processing of Gli3 produces an anterior/posterior repressor gradient in the developing vertebrate limb. *Cell* **100**, 423 (2000). doi:10.1016/S0092-8674(00)80678-9 Medline

4. Y. Litingtung, R. D. Dahn, Y. Li, J. F. Fallon, C. Chiang, Shh and Gli3 are dispensable for limb skeleton formation but regulate digit number and identity. *Nature* **418**, 979 (2002). doi:10.1038/nature01033 Medline

5. P. te Welscher *et al*., Progression of vertebrate limb development through SHH-mediated counteraction of GLI3. *Science* **298**, 827 (2002). doi:10.1126/science.1075620 Medline

6. S. Kondo, T. Miura, Reaction-diffusion model as a framework for understanding biological pattern formation. *Science* **329**, 1616 (2010). doi:10.1126/science.1179047 Medline

7. A. M. Turing, The chemical basis of morphogenesis. *Philos. Trans. R. Soc. London Ser. B.* **237**, 37 (1952). doi:10.1098/rstb.1952.0012

8. S. A. Newman, H. L. Frisch, Dynamics of skeletal pattern formation in developing chick limb. *Science* **205**, 662 (1979). doi:10.1126/science.462174 Medline

9. A. Gierer, H. Meinhardt, A theory of biological pattern formation. *Kybernetik* **12**, 30 (1972). doi:10.1007/BF00289234 Medline

10. T. Miura, K. Shiota, G. Morriss-Kay, P. K. Maini, Mixed-mode pattern in Doublefoot mutant mouse limb—Turing reaction-diffusion model on a growing domain during limb development. *J. Theor. Biol.* **240**, 562 (2006). doi:10.1016/j.jtbi.2005.10.016 Medline

11. P. K. Maini, M. Solursh, Cellular mechanisms of pattern formation in the developing limb. *Int. Rev. Cytol.* **129**, 91 (1991). doi:10.1016/S0074-7696(08)60510-0 Medline

12. S. A. Newman, Sticky fingers: *Hox* genes and cell adhesion in vertebrate limb development. *Bioessays* **18**, 171 (1996). doi:10.1002/bies.950180302 Medline

13. J. Zákány, D. Duboule, Hox genes in digit development and evolution. *Cell Tissue Res.* **296**, 19 (1999). doi:10.1007/s004410051262 Medline

14. J. Zákány, M. Kmita, D. Duboule, A dual role for *Hox* genes in limb anterior-posterior asymmetry. *Science* **304**, 1669 (2004). doi:10.1126/science.1096049 Medline

15. M. Kmita *et al*., Early developmental arrest of mammalian limbs lacking *HoxA*/*HoxD* gene function. *Nature* **435**, 1113 (2005). doi:10.1038/nature03648 Medline

16. Y. Chen *et al*., Direct interaction with Hoxd proteins reverses Gli3-repressor function to promote digit formation downstream of Shh. *Development* **131**, 2339 (2004). doi:10.1242/dev.01115 Medline

17. M. Kmita, N. Fraudeau, Y. Hérault, D. Duboule, Serial deletions and duplications suggest a mechanism for the collinearity of *Hoxd* genes in limbs. *Nature* **420**, 145 (2002). doi:10.1038/nature01189 Medline

18. C. Fromental-Ramain *et al*., Hoxa-13 and Hoxd-13 play a crucial role in the patterning of the limb autopod. *Development* **122**, 2997 (1996). Medline

19. J. Zákány, C. Fromental-Ramain, X. Warot, D. Duboule, Regulation of number and size of digits by posterior *Hox* genes: A dose-dependent mechanism with potential evolutionary implications. *Proc. Natl. Acad. Sci. U.S.A.* **94**, 13695 (1997). doi:10.1073/pnas.94.25.13695 Medline

20. A. P. Davis, M. R. Capecchi, A mutational analysis of the 5′ HoxD genes: Dissection of genetic interactions during limb development in the mouse. *Development* **122**, 1175 (1996). Medline

21. D. J. Goff, C. J. Tabin, Analysis of Hoxd-13 and Hoxd-11 misexpression in chick limb buds reveals that Hox genes affect both bone condensation and growth. *Development* **124**, 627 (1997). Medline

22. V. Knezevic *et al*., Hoxd-12 differentially affects preaxial and postaxial chondrogenic branches in the limb and regulates Sonic hedgehog in a positive feedback loop. *Development* **124**, 4523 (1997). Medline

23. R. Sheth, M. F. Bastida, M. Ros, Hoxd and Gli3 interactions modulate digit number in the amniote limb. *Dev. Biol.* **310**, 430 (2007). doi:10.1016/j.ydbio.2007.07.023 Medline

24. E. McGlinn *et al*., Pax9 and Jagged1 act downstream of Gli3 in vertebrate limb development. *Mech. Dev.* **122**, 1218 (2005). doi:10.1016/j.mod.2005.06.012 Medline

25. T. Miura, P. K. Maini, Speed of pattern appearance in reaction-diffusion models: implications in the pattern formation of limb bud mesenchyme cells. *Bull. Math. Biol.* **66**, 627 (2004). doi:10.1016/j.bulm.2003.09.009 Medline

26. J. Lopez-Rios *et al*., GLI3 constrains digit number by controlling both progenitor proliferation and BMP-dependent exit to chondrogenesis. *Dev. Cell* **22**, 837 (2012). doi:10.1016/j.devcel.2012.01.006 Medline

27. R. D. Dahn, M. C. Davis, W. N. Pappano, N. H. Shubin, Sonic hedgehog function in chondrichthyan fins and the evolution of appendage patterning. *Nature* **445**, 311 (2007). doi:10.1038/nature05436 Medline

28. M. C. Davis, R. D. Dahn, N. H. Shubin, An autopodial-like pattern of Hox expression in the fins of a basal actinopterygian fish. *Nature* **447**, 473 (2007). doi:10.1038/nature05838 Medline

29. R. Freitas, G. Zhang, M. J. Cohn, Biphasic *Hoxd* gene expression in shark paired fins reveals an ancient origin of the distal limb domain. *PLoS ONE* **2**, e754 (2007). doi:10.1371/journal.pone.0000754 Medline

30. J. M. Woltering, D. Duboule, The origin of digits: expression patterns versus regulatory mechanisms. *Dev. Cell* **18**, 526 (2010). doi:10.1016/j.devcel.2010.04.002 Medline

31. I. Schneider *et al*., Appendage expression driven by the *Hoxd* Global Control Region is an ancient gnathostome feature. *Proc. Natl. Acad. Sci. U.S.A.* **108**, 12782 (2011). doi:10.1073/pnas.1109993108 Medline

32. N. Shubin, C. Tabin, S. Carroll, Deep homology and the origins of evolutionary novelty. *Nature* **457**, 818 (2009). doi:10.1038/nature07891 Medline

33. M. A. Nieto, K. Patel, D. G. Wilkinson, In situ hybridization analysis of chick embryos in whole mount and tissue sections. *Methods Cell Biol.* **51**, 219 (1996). doi:10.1016/S0091-679X(08)60630-5 Medline

34. B. Boehm *et al*., A landmark-free morphometric staging system for the mouse limb bud. *Development* **138**, 1227 (2011). doi:10.1242/dev.057547 Medline

35. www.vtk.org/

36. R. A. Barrio, C. Varea, J. L. Aragón, P. K. Maini, A two-dimensional numerical study of spatial pattern formation in interacting Turing systems. *Bull. Math. Biol.* **61**, 483 (1999). doi:10.1006/bulm.1998.0093 Medline

37. B. Boehm *et al*., The role of spatially controlled cell proliferation in limb bud morphogenesis. *PLoS Biol.* **8**, e1000420 (2010). doi:10.1371/journal.pbio.1000420 Medline

38. C. Geuzaine, J. Remacle, Gmsh: A 3-D finite element mesh generator with built-in pre- and post-processing facilities. *Int. J. Numer. Methods Eng.* **79**, 1309 (2009). doi:10.1002/nme.2579

39. T. Glimm, J. Zhang, Y. Q. Shen, S. A. Newman, Reaction-diffusion systems and external morphogen gradients: the two-dimensional case, with an application to skeletal pattern formation. *Bull. Math. Biol.* **74**, 666 (2012). doi:10.1007/s11538-011-9689-6 Medline

40. P. K. Maini, in *Developmental Patterning of the Vertebrate Limb* (Plenum Press, New York, 1991), pp. 161–163.

41. P. K. Maini, D. L. Benson, J. A. Sherratt, Pattern formation in reaction diffusion models with spatially inhomogeneous diffusion coefficients. *IMA J. Math. Appl. Med. Biol.* **9**, 197 (1992). doi:10.1093/imammb/9.3.197

42. L. Marjoram, C. Wright, Rapid differential transport of Nodal and Lefty on sulfated proteoglycan-rich extracellular matrix regulates left-right asymmetry in Xenopus. *Development* **138**, 475 (2011). doi:10.1242/dev.056010 Medline

43. J. D. Murray, *Mathematical Biology* (Springer, Berlin, 1993).

44. P. Müller *et al*., Differential diffusivity of Nodal and Lefty underlies a reaction-diffusion patterning system. *Science* **336**, 721 (2012). doi:10.1126/science.1221920 Medline

45. H. Shoji, Y. Iwasa, Labyrinthine versus straight-striped patterns generated by two-dimensional Turing systems. *J. Theor. Biol.* **237**, 104 (2005). doi:10.1016/j.jtbi.2005.04.003 Medline

46. H. Shoji, Y. Iwasa, A. Mochizuki, S. Kondo, Directionality of stripes formed by anisotropic reaction-diffusion models. *J. Theor. Biol.* **214**, 549 (2002). doi:10.1006/jtbi.2001.2480 Medline